Energy performance advantages of using multiple compressors in a heat pump operating in heating mode

Geoffrey Viviescas, Houaida Saidi, Michel Bernier, Michael Kummert
Polytechnique Montréal

Abstract

The energy performance of a multi-compressor geothermal heat pump (MC-GHP) is investigated in this study. The MC-GHP is equipped with eight compressors of different capacities and efficiencies. In operation, the compressor having the lowest energy consumption (compressor power + auxiliary heating) at a given time step is selected. The objective is to determine, through simulations over three winter months, the difference in the Seasonal Coefficient of Performance (SCOP) of the MC-GHP compared to a regular single compressor geothermal heat pump.

In the first part of the paper, a complete steady-state model of a water-to-water MC-GHP is developed. Heat transfer is modelled from first principles in the evaporator and condenser plate heat exchangers. Detailed manufacturer performance maps based on the AHRI 540-2015 standard are used to model the performance of the compressors. Performance degradation caused by heat pump cycling is handled using a part-load-factor approach.

Results show that the SCOP of the MC-GHP is 13.3% higher that the SCOP obtained with a single compressor geothermal heat pump.

Introduction

Basic thermodynamics tells us that the coefficient of performance (COP) of a reversible Carnot heat pump (HP) depends on the difference between the source and sink temperatures; small temperature differences lead to high COPs.

In a real heat pump operating in heating mode, the source is typically the outside air or the ground and the sink is typically either the inside air in the case of space heating or hot water for domestic hot water heating. Heat exchangers are required between the source and the refrigerant in the evaporator and between the sink and the refrigerant in the condenser. Because of the finite heat transfer area of the heat exchangers, there is a temperature difference between the refrigerant and the secondary fluids. This temperature difference is typically of the order of 5 K. Thus, for example, for source and sink temperatures of 0 and 20 ℃ the refrigerant temperatures in the evaporator and condenser are -5 and 25 ℃, respectively. The source/sink temperature difference is then increased from 20 to 30 K because of the finite heat transfer area.

Compressor inefficiencies also contribute to reducing heat pump COP. Figure 1 presents curves of isentropic efficiencies η_{is} for three commercially available compressors (which will be used later in this study). As shown on this figure, η_{is} depends on the compressor model, the evaporating pressure and the pressure ratio (ratio of the refrigerant pressures prevailing in the condenser and in the evaporator). This pressure ratio (PR) is proportional to the source/sink temperature difference. As can be seen, each compressor curve peaks at a different pressure ratio. Thus, as the source/sink temperature difference evolves during a heating season, the value of η_{is} might be significantly lower than its peak value. For example, for an evaporating pressure of 460 kPa, compressor #2 has a better isentropic efficiency for PR values between 2 and 3, while for a PR between 3 and 4, compressor #3 has a better efficiency and finally for PR greater than 4, compressor #4 has the highest isentropic efficiency. Thus, it might be advantageous to switch from one compressor to the other during a heating season to maximize the annual seasonal COP of a heat pump. Figure 1 also shows that the variation of η_{is} is dependent on the evaporating pressure. For example, for compressor #4, the curve for η_{is} is lower for an evaporating pressure of 320 kPa.
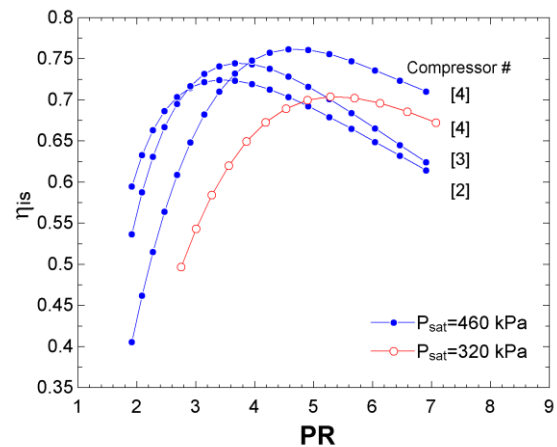
Figure 1 Isentropic efficiencies for three compressors as a function of the pressure ratio (PR) for two evaporating pressures

Aside from efficiency, the variation of heat pump capacity is an important factor in compressor selection. Low source temperatures reduce the density of the refrigerant leaving the evaporator and entering the compressor. In turn, this reduces the refrigerant mass flow rate in the circuit and the heating capacity at the condenser. For example, the vapour density of saturated R-407C varies from 37.54 to 16.52 kg/m^3 when the temperature decreases from +20 to -5 °C, a 56% drop in density. Thus, if everything remains unchanged, this change in density leads to a 56% drop in capacity.

If the heating demand of the system is lower than the HP capacity, it will operate in cycling mode (part load) with associated losses in performance. On the other hand, if the heating capacity is lower than the building heating load, auxiliary heating, typically resistance heating, is required.

A HP with multiple compressors with different capacities and efficiencies (i.e. different η_{is} vs PR curves) may thus lead to a better energy performance than a standard single-compressor HP. The development of new technologies in the design of miniature centrifugal compressors (Arpagaus et al. 2017; Schiffmann 2014), along with advances in 3D printing technology (Michaud et al. 2019) could significantly reduce capital costs associated with manufacturing and installing multiple compressors in commercial and residential heat pumps. A schematic of such an arrangement is shown in Figure 2 where the components of the MC-GHP are enclosed within the dotted line. In this study a total of eight compressors are linked in parallel to the evaporator and condenser; only one operates at any given time. In the case presented in Figure 2, compressor #4 is used when the house heating load is 9.9 kW. The various temperatures shown in Figure 2 are obtained from the model presented here at t =100 hours.
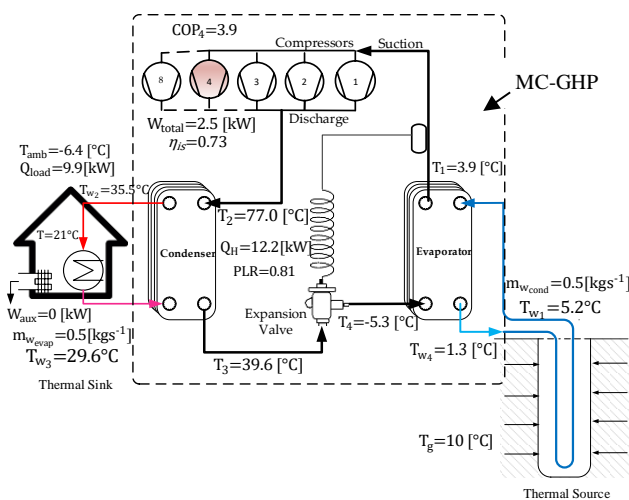
Figure 2 Schematic representation of a multi-compressor heat pump

Literature review

Shen et al. (2016) developed an air-source cold climate heat pump (CCHP), which uses tandem compressors, with each compressor rated to meet the building design cooling load. The CCHP maintained an acceptable comfort level throughout the heating season. In comparison to a single-speed heat pump, the CCHP demonstrated more than 40% energy savings in the peak heating month.

Shen et al. (2019) also developed a prototype air-source cold climate heat pump, using tandem vapor injection compressors and inter-stage flash tanks. The CCHP has two identical compressors in parallel and works with a two-stage indoor blower and is controlled with a two-stage thermostat. At moderately low ambient temperatures, only one compressor is called, and at extremely low ambient temperatures, both compressors are used. They concluded that the seasonal performance is 5% higher than using just tandem, single-speed compressors without vapor injection and flash tanks. Hu et al. (2019) performed simulations of a heat pump equipped with a centrifugal compressor used for waste heat recovery and compared the system performance of three configurations : one-cycle two-compressor system, two-compressor parallel system, and two-cycles parallel system. Results show that the two-cycle parallel system is advantageous in terms of heating capacity and COP. The COP of the two-compressor parallel system is 6.5% higher than the one cycle compressor system under the same working conditions.

Conventional air-source heat pumps (ASHPs) experience rather poor performance in cold climates. The heating capacity and COP decrease significantly as the outdoor temperature decreases. The major R&D challenges are to limit the decrease in heating capacity and COP at low ambient temperatures (Shen et al. 2019). The work presented here attempts to alleviate this problem by first proposing to use a multi-compressor geothermal heat pump which does not experience low ambient air temperature and which can adapt its capacity by changing the compressor being used.

The proposed MC-GHP configuration is equipped with eight compressors (Figure 2). A specific compressor is selected for a given set of operating conditions to minimize heat pump energy consumption (compressor power and auxiliary heating).

Methodology

The heat pump performance information supplied by manufacturers is usually based on simplified operating conditions. Developing a complete heat pump model based on first principles, allows to evaluate each component of the heat pump individually and incorporate new technologies in the cycle if required.

Hourly simulations are performed on the system presented in Figure 2 which shows three main components: building,

MC-GHP, and ground heat exchanger. Models used for the building and the ground heat exchanger will be briefly presented while the MC-GHP model will be described in detail.

Each component is modeled within the Engineering Equation Solver (EES, 2020) software tool. The main reason for this selection is the capabilities offered by EES to solve simultaneously the governing equations of the MC-GHP model including the determination of the refrigerant properties.

Building model

A single zone building, maintained at a constant temperature, T_{int}, is assumed The hourly building load, Q_{load}, is simply calculated using Equation 1.

$$Q_{load} = UA \times (T_{int} - T_{ext}) - Q_{gains} \qquad (1)$$

where UA is the building loss coefficient, T_{ext} is the ambient temperature and Q_{gains} are the internal heat gains. It is assumed in this study that UA and Q_{gains} are constant.

Ground heat exchanger model

The model used for the ground heat exchanger has been described by Saidi (2019). It uses the Cylindrical Heat Source analytical solution to obtain the borehole wall temperature at a given time step j, $T_{b,j}$, as a function of the ground load and undisturbed ground temperature. As noted by Saidi (2019), the thermal history of ground heat extraction is accounted for using a temporal superposition scheme. The hourly mean fluid temperature, $T_{m,j}$, is then obtained assuming a constant borehole thermal resistance, R_b, using Equation 2:

$$T_{m,j} = T_{b,j} - Q_{ground,load,j} \times R_b \qquad (2)$$

where $Q_{ground,load,j}$ is the ground heat extraction load at time step j. It is assumed that borehole thermal capacity effects are negligible and thus $Q_{ground,load,j}$ is equal to the heat transferred in the evaporator ($Q_{T,evap}$ in Equation 29).

Heat Pump Model

One of the important contribution of this work is the MC-GHP model which will now be described in detail.

Compression heat pumps are composed of four basic components: condenser, evaporator, expansion valve and compressor. The thermodynamic cycle of such heat pumps is presented in Figure 3 on a Pressure-Enthalpy (P-h) diagram for R407C which is the refrigerant used in the present study. The refrigerant leaves the evaporator as a superheated vapor at a temperature T_1 and exists the compression process at T_2. In the condenser, the refrigerant is first de-superheated from T_2 to $T_{x,2}$ and then condensed down to a saturated liquid at T_3. Note that $T_{x,2} \neq T_3$ when a

zeotropic refrigerant such as R407C is used. Then, there is an isenthalpic pressure drop in the expansion valve and the refrigerant enters the evaporator at T_4. In the evaporator, the refrigerant undergoes an evaporation from T_4 to $T_{x,1}$ and is then superheated up to T_1. A temperature sensing device located at the exit of the evaporator (see Figure 2) controls the expansion valve opening until the required degree of superheat is obtained (typically 5 K).
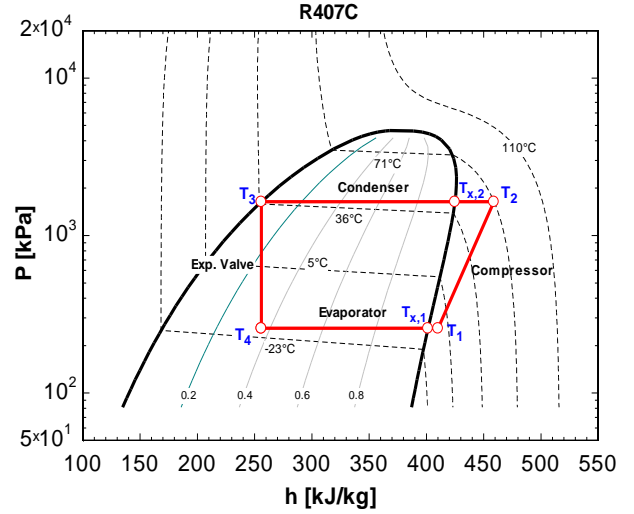
Figure 3 Typical P-h diagram for R407C

The model uses four inputs associated with the secondary fluids (see Figure 2): inlet temperatures and flow rates at the evaporator and condenser, T_{w_3}, T_{w_1}, $\dot{m}_{w_{evap}}$, and $\dot{m}_{w_{cond}}$, respectively. Thus, the shape of the red polygon in Figure 3 changes as the input conditions change over the heating season.

A detailed description of the sub-models of each component will now be presented.

Compressor

The published rating of compressors are standardized under the CAN/ANSI/AHRI 540-2015 standard (AHRI 2015). The nominal characteristics given by the manufacturers are the compressor power in Watts and the refrigerant mass flow in kg.s^{-1}. These data are in the form of third order polynomial equation with 10 coefficients as shown in Equation 3:

$$X = C_1 + C_2 T_S + C_3 T_D + C_4 T_S^2 + C_5 T_D T_S + C_6 T_D^2 + C_7 T_S^3 + C_8 T_D T_S^2 + C_9 T_S T_D^2 + C_{10} T_D^3 \qquad (3)$$

where:
C_1 to C_{10} = regression coefficients provided by the manufacturer
T_D = discharge dew point temperature, °C ($T_{x,2}$ in Figure 3)
T_S = suction dew point temperature, °C ($T_{x,1}$ in Figure 3)
X = power input (W) or refrigerant mass flow (kg s^{-1})

Equation 3 is valid for both zeotropic (with a temperature glide) as well as azeotropic refrigerant. The compressor sizes were chosen in such a way as to cover a wide range of loads while having efficiency peaks in different pressure ratios based on the operating conditions. The characteristics of the eight compressors selected in this study are shown in Appendix A and correspond to commercially available compressors.

Condenser and evaporator modeling

Both the condenser and evaporator of the MC-GHP use plate heat exchangers (PHEs). Figures 4 and 5 present schematically the plate arrangements while Table 1 presents the geometry used in the present study.
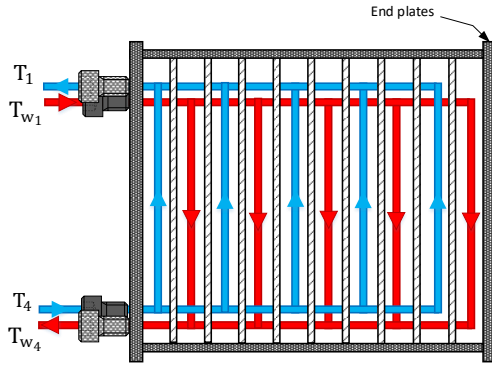
Figure 4 Schematic of the plate heat exchangers used in the condenser and evaporator
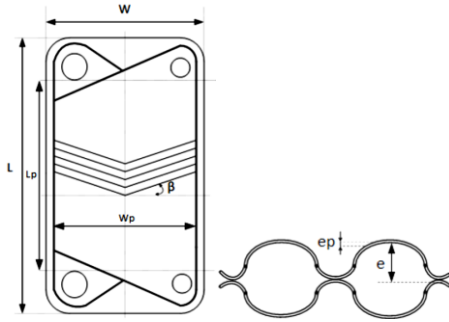
Figure 5 Diagram of a plate exchanger and cross section of two adjacent plates

Table 1 Plate heat exchanger characteristics

Parameter	Value	Units
W × L	100×500	mm × mm
Chevron angle, β	45	°
Plate thickness, t_p	0.4	mm
Plate spacing, e	2	mm
Hydraulic diameter, $D_H (= 2e)$	4	mm
Effective surface area, A_p	0.052	m²/plaque
Number of plates in evaporator, NP	25	-
Number of plates in condenser, NP	25	-
Plate thermal conductivity, k_p	380	W/m-K

The PHEs operate in steady state and their outside surface is adiabatic. The main flow is assumed to be divided equally among all channels. The velocity profile in the channels is assumed to be flat (plug flow) and perfect mixing occurs at the exit of every channel. Both condenser and evaporator are modeled using the $\varepsilon - NTU$ method for heat exchangers (Bergman et al., 2011). The determination of the NTU requires the evaluation of the overall heat transfer coefficient UA calculated using Equations 4 and 5.

The total heat transfer area is given by:

$$A = (N_c - 1)A_p \tag{4}$$

where N_c is the number of channels in the PHE. The end plates are adiabatic and are not taken into account in the total heat transfer area. The overall heat transfer coefficient can be determined by:

$$U = \frac{1}{\frac{1}{h_{hot}} + \frac{t_p}{k_p} + \frac{1}{h_{cold}} + R_{f,cold} + R_{f,hot}} \tag{5}$$

where

h_{hot} = convective heat transfer coefficient on the hot fluid side

h_{cold} = convective heat transfer coefficient on the cold fluid side

$R_{f,hot}$ = fouling factor on the hot fluid side

$R_{f,cold}$ = fouling factor on the cold fluid side

It is assumed that fouling is negligible and both $R_{f,hot}$ and $R_{f,cold}$ are set to zero.

The determination of the convective heat transfer coefficients in the PHEs is difficult because two different heat transfer processes occur in both heat exchangers: a region of two-phase flow (evaporation or condensation) and single-phase flow (superheating or desuperheating).

Due to the wide range of plate designs, there are various parameters and correlations available for heat transfer coefficients. Most of them are expressed as a function of the Reynolds number (Re), the Prandtl number (Pr), the surface enlargement factor (ϕ) and the chevron angle (β). In some cases involving phase change, the quality (x) and heat transfer rate (Q), are also required.

In this work, the Wanniarachchi et al. (1995) correlation is used for single-phase heat transfer (superheated process) while the Yan et al. (1999) and Cooper (1984) relationships are used for condensation and evaporation, respectively. Note that some of the terms presented below are defined in the nomenclature.

Single Phase: For the calculation of the heat transfer coefficient in single phase, the modified Wanniarachchi correlation (Kim and Park 2017; Wanniarachchi et al. 1995) is used to determine the Nusselt (Nu) number:

$$Nu = \left(Nu_l^3 + Nu_l^3\right)^{\frac{1}{3}} Pr^{\frac{1}{3}} \left(\mu/\mu_w\right)^{0.17} \tag{6}$$

$$Nu_l = 3.65\phi^{0.661}Re^{0.339}/(90 - \beta)^{0.455} \tag{7}$$

$$Nu_t = 12.6\phi^{1-m}Re^m/(90-\beta)^{1.142} \qquad (8)$$

$$m = 0.646 + 0.0011(90-\beta) \qquad (9)$$

Condensation: For the calculation of the heat transfer coefficient by condensation, the model of Yan et al. (1999) is used:

$$Nu = \frac{h_{tp}D_h}{k_t} = 4.118Re_{eq}^{0.4}Pr^{0.333} \qquad (10)$$

$$Re_{eq} = \frac{G_{eq}D_h}{\mu_l} \qquad (11)$$

$$G_{eq} = G\left[1 - X_m + X_m\left(\frac{\rho_l}{\rho_v}\right)\right] \qquad (12)$$

Evaporation: García-Cascales et al. (2007) observed that in the case of evaporation, the model presented by Cooper (1984) is in good agreement with the experimental results and it was therefore selected for the present study. It is simply given by:

$$\frac{h}{(q/A)^{0.67}} = 55P_r^{[0.12-0.2log_{10}R_p]}(-logP_r)^{-55}M^{-0.5} \qquad (13)$$

Figure 6 shows the overall heat transfer coefficient U obtained for the evaporator and condenser described in Table 1. These results were obtained using Equation 5 and the individual coefficients calculated with Equations 6 to 13 for three different compressors (i.e. three different nominal refrigerant flow rates) for a sub-set of the data for the three month simulation period. Figure 6 shows that the value of U ranges from ~1.0 to ~1.5 kW/m²-K and that its value is almost independent of the ambient temperature.
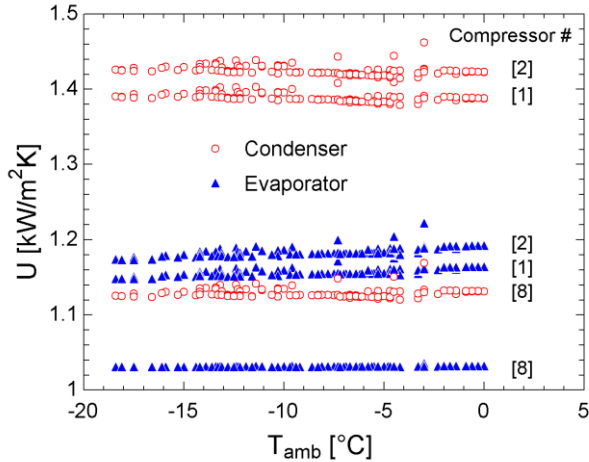
Figure 6 Global heat transfer coefficients in the evaporator and condenser extracted from hourly simulations

Condenser heat transfer model: The total heat transferred in the condenser, $Q_{T,cond}$, is equal to the sum of the heat transferred in the superheat zone, Q_{sh_c} and the heat transferred by condensation, Q_{cond}, as shown in Figure 7.
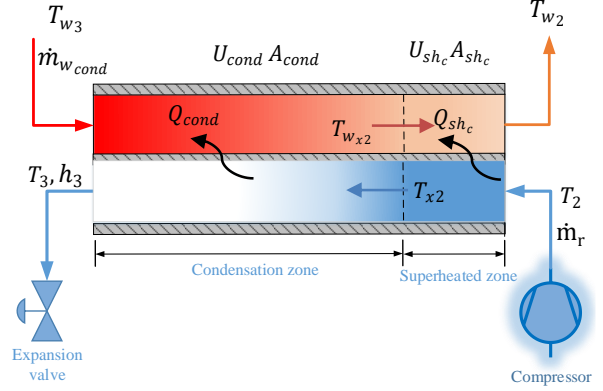
Figure 7 Schematic representation of the condenser

The model does not include a sub-cooling zone as it is assumed that the refrigerant leaves the condenser as a saturated liquid.

$$Q_{T,cond} = Q_{cond} + Q_{sh_c} \qquad (14)$$

$$Q_{T,cond} = \dot{m}_{w_{cond}}C_{p,w}(T_{w_2} - T_{w_3}) \qquad (15)$$

The additional energy balance equations are:

$$Q_{cond} = \dot{m}_{w_{cond}}C_{p,w}\left(T_{w_{x_2}} - T_{w_3}\right) \qquad (16)$$

$$Q_{sh_c} = \dot{m}_r C_{p,r}(T_2 - T_{x_2}) \qquad (17)$$

These heat transfer rates are also given by:

$$Q_{cond} = \varepsilon_{cond}c_{min}(T_{x_2} - T_{w_3}) \qquad (18)$$

$$Q_{sh_c} = \varepsilon_{sh_c}c_{min}\left(T_2 - T_{w_{x_2}}\right) \qquad (19)$$

Where the effectiveness (ε) is define as the ratio of the actual heat transfer rate Q to the maximum possible heat transfer rate, Q_{max}:

$$\varepsilon = \frac{Q}{Q_{max}} \qquad (20)$$

The effectiveness for evaporation or condensation can be calculated from equation.

$$\varepsilon_{cond} = 1 - e(-NTU_{cond}) \qquad (21)$$

However, for latent heating ε depends on geometric factors and fluid thermal capacities. The effectiveness is then given by:

$$\varepsilon_{sh_c} = \frac{1 - e^{[(-NTU_{sh_c})(1-C_r)]}}{1 - C_r e^{[(-NTU_{sh_c})(1-C_r)]}} \qquad (22)$$

$$c_{min} = min(\dot{m}_r C_{p,r}, \dot{m}_w C_{p,w}) \qquad (23)$$

$$c_{max} = max(\dot{m}_r C_{p,r}, \dot{m}_w C_{p,w}) \qquad (24)$$

$$C_r = \frac{c_{min}}{c_{max}} \qquad (25)$$

where $\dot{m}_w C_{p,r}$ and $\dot{m}_r C_{p,w}$ are the water and refrigerant thermal capacities, respectively. For evaporation or condensation processes, $c_{max} \sim \infty$ and therefore $C_r = 0$.

The *NTU* values are obtained using:

$$NTU_{sh_c} = \frac{U_{sh_c} A_{sh_c}}{c_{min}} \qquad (26)$$

$$NTU_{cond} = \frac{U_{cond} A_{cond}}{c_{min}} \qquad (27)$$

The outlet temperature of the secondary fluid from the condenser, T_{w_2}, is used for house heating. Its value is set as a function of the ambient temperature with a simple linear relationship that represents a conventional supply temperature adjustment known as "outdoor temperature reset" for a low-temperature heating system:

$$T_{w_2} = -0.375 \times T_{amb} + 32 \qquad (28)$$

where all temperatures are in °C.

Evaporator heat transfer model: The model for the evaporator is similar to the one used for the condenser. It is assumed that the heat pump operates with 5 K of superheat. As can be seen in Figure 8, total heat transfer in the evaporator, $Q_{T,evap}$, is equal to the sum of the heat transferred in the evaporation section, Q_{evap}, and in the superheated zone, Q_{sh_e}. The governing equations are as follows:

$$Q_{T,evap} = Q_{evap} + Q_{sh_e} \qquad (29)$$

$$Q_{T,evap} = \dot{m}_{w_{evap}} C_{p,w} (T_{w_1} - T_{w_4}) \qquad (30)$$
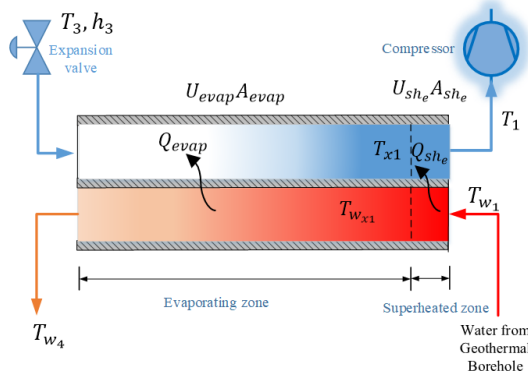
Figure 8 Schematic representation of the evaporator

$$Q_{evap} = \dot{m}_w C_{p,w} \left(T_{w_{x_1}} - T_{w_4} \right) \qquad (31)$$

$$Q_{sh_e} = \dot{m}_r C_{p,r} (T_1 - T_{x_1}) \qquad (32)$$

Equations similar to Equations 20 to 27 are applied to the evaporator.

The condenser model has been verified against data from a manufacturer of PHEs. Table 2 presents the results of this verification on four PHE models. On the refrigeration side, the condensation temperature is 50 °C with an inlet temperature (from the compressor) of 90 °C. The inlet and outlet water temperatures are 40 and 45 °C, respectively. As can be seen, the agreement is relatively good with a maximum difference of 15% which is considered acceptable

considering the uncertainty in the determination of the heat transfer coefficients.

Table 2 Verification of the condenser model

Model	L [m]	W [m]	A_p [m^2]	NP	Q_{cond} manufacturer [kW]	Q_{cond} model [kW]
B3-23	0.315	0.073	0.023	22	2.5	2.9
B3-32	0.286	0.116	0.032	32	5.0	5.1
B3-52	0.523	0.107	0.052	30	12.5	12.1
B3-95	0.616	0.191	0.095	26	30	34.7

*Thermal expansion valve model***:**

The process from T_3 to T_4 is isenthalpic and thus:

$$h_4 = h_3 \qquad (33)$$

Global model

As indicated earlier, the model uses the inlet conditions of the two secondary fluids as inputs. Each of the four models described above are coupled together and need to be solved simultaneously with EES for each of the eight compressors. EES often requires several iterations and the choice of the guess values is important to obtain convergence. In this work, the guess values used at the start of a given time step are the converged values from the previous time step. Hourly simulations over a three month period requires approximately 3 hours of computation time on up-to-date desktop computer.

Heat pump cycling losses are handled using the part load factor/part load ratio (FLF/PLR) approach proposed by Fuentes et al. (2016) which is based on an experimental study carried out to characterize the behaviour of water-to-water heat pumps that operate under partial load. The PLF/PLR for compressor i at time step j are obtained using the following equations:

$$PLF_{ij} = \frac{1}{1 + \dfrac{C_d(1 - PLR_{ij})}{1 - C_d(1 - PLR_{ij})} + (1 - C_c)\dfrac{1 - PLR_{ij}}{PLR_{ij}}} \qquad (34)$$

$$PLR_{ij} = min \left[1, \frac{Q_{load_j}}{Q_{H,i,j}} \right] \qquad (35)$$

where C_d (= 0.22) and C_c (= 0.998) are start-up and stand-by degradation coefficients, $Q_{H,i,j}$ is the heat supplied by the heat pump i (i.e. its capacity) at time step j. The resulting heat pump power consumption, $W_{net,r,i,j}$, is given by:

$$W_{net,r,i,j} = W_{net,i,j} \frac{PLR_{ij}}{PLF_{ij}} \qquad (36)$$

where $W_{net,i,j}$ is evaluated using Equation 1 with coefficients from Tables A-1 and A-2.

At each time step, a modified COP value of each compressor is evaluated using:

$$COP_{mod,i,j} = \frac{Q_{load_j}}{W_{net,r,ij} + W_{aux,ij}} \qquad (37)$$

where the amount of auxiliary heating is defined as:

$$W_{aux,i,j} = max(Q_{load_j} - Q_{H,i,j}, 0) \qquad (38)$$

The compressor giving the highest value of $COP_{mod,i,j}$ is selected at every time-step.

Finally, the seasonal coefficient of performance for compressor i, $SCOP_i$, is evaluated using equation 39.

$$SCOP_i = \frac{\sum_{j=1}^{n} Q_{Load_j}}{\sum_{j=1}^{n}(W_{net,r,i,j} + W_{aux,i,j})} \qquad (39)$$

where n is the number of hours of the simulation.

Results and discussions

The energy performance simulations of a multi-compressor geothermal heat pump (MC-GHP) for a three-month period (starting on January 1st) are reported and discussed in this section. The building and ground heat exchanger parameters are given in Table 3 while the PHE characteristics are presented in Table 1. Hourly simulations are performed using the Montréal weather.

Table 3 Parameters of the building and geothermal heat exchanger

Parameter	Value	Units
Building loss coefficient, UA	0.4	[kW.K^{-1}]
Set point temperature, T_{int}	21	[°C]
Internal heat gains, Q_{gains}	1	[kW]
Ground heat exch. length, L_{bh}	600	[m]
Borehole diameter, D_{bh}	0.15	[m]
Ground thermal conductivity, k_{bh}	2.5	[W.m^{-1}°.C^{-1}]
Ground thermal diffusivity, α_{bh}	0.1	[m^2.day^{-1}]
Undisturbed ground temp, T_g	10	[°C]
Borehole thermal resistance, R_b	0.1	[m.°C.W^{-1}]

Figure 9 shows that the building load varies from ~5 to ~ 19 kW during the three-month simulation period. As expected, the variations of the borehole outlet temperature and return water temperature from the condenser follow the peak and valleys of the building loads. Variations are sometimes abrupt but the global model is able to converge despite these relatively steep changes in the secondary fluid temperatures.
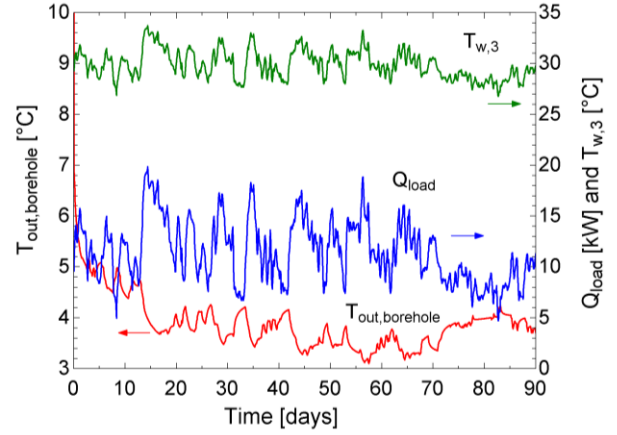
Figure 9 Building load, borehole outlet temperature, and return temperature from the condenser

Figure 10 shows the behavior of compressor #1 over the three-month period. The value of COP_{mod} and PLR are plotted as a function of the hourly building load. For $Q_{load} >$ 14.5 kW, the capacity of the compressor is insufficient to meet the load and auxiliary heating is required which explains the decrease in the value of COP_{mod} from ~ 3.4 down to ~ 2.2. For $Q_{load} <$ 14.5 kW, the capacity is larger than the load and the PLR decreases which leads to a degradation of the performance with COP_{mod} values decreasing from ~ 3.4 to ~ 3.2.
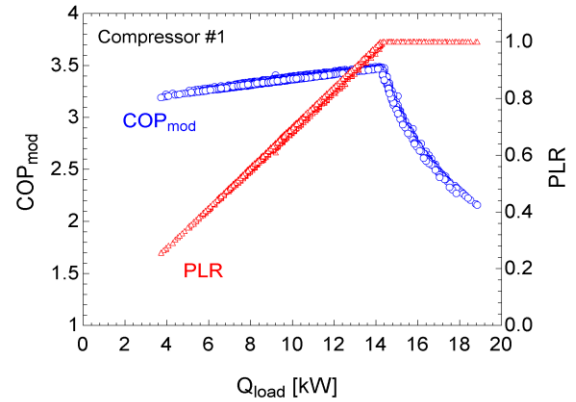
Figure 10 COP_{mod} and PLR for compressor #1 over the three-month period

Figure 11 shows the values of COP_{mod} for all eight compressors for the entire three-month period as a function of the ambient temperature. In addition, the best COP_{mod} value obtained at each time step is indicated in the figure by a solid line. The COP_{mod} curves show a pattern similar to the one shown in Figure 10. Clearly, some compressors have better COP_{mod} than others because their capacity corresponds more closely to the building load. Table 4 gives the compressor with the highest COP_{mod} for a given ambient temperature range. It is to be noted that compressor #6 is not selected during the three-month period.
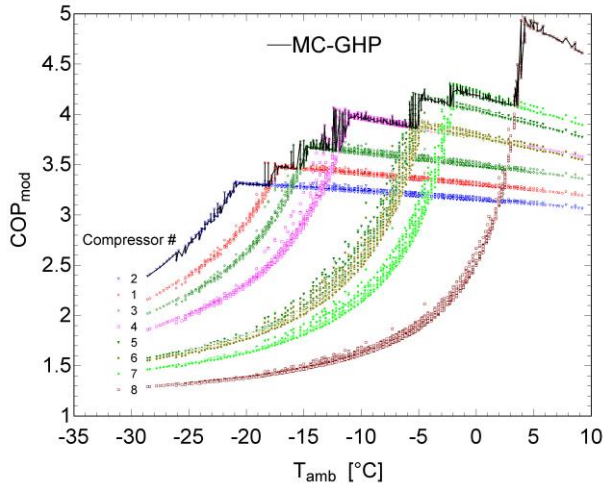
Figure 11 Variation of COP_{mod} for all compressors and the MC-GHP as a function of ambient temperature

Table 4 Compressor selection as a function of ambient temperature range

Approximate ambient temperature range	Compressor with the highest COP_{mod}
-29°C to -18°C	2
-18°C to -16°C	1
-16°C to -13°C	3
-12°C to -7°C	4
-6°C to -2°C	5
-2°C to 3°C	7
> 3°C	8

Figure 12 shows the *SCOP* for each of the 8 compressors and the *SCOP* obtained for the MC-GHP. A minimum *SCOP* of 1.72 is obtained for compressor #8 and a maximum of 3.31 for compressor #3. The MC-GHP has a *SCOP* of 3.75, which represents a 13.3% improvement over the best compressor.
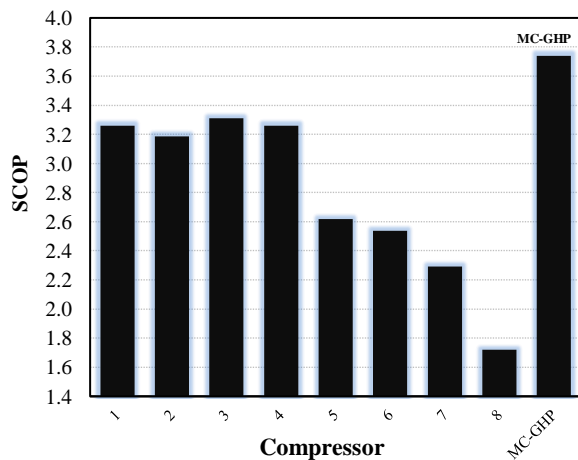
Figure 12 Seasonal coefficient of performance (SCOP) for each compressor and for the MC-GHP

Conclusion

The energy performance of a multi-compressor water-to-water geothermal heat pump (MC-GHP) is investigated in this study. The MC-GHP is equipped with eight compressors of different capacities and efficiencies. In operation, the compressor that leads to the lowest energy consumption (compressor power + auxiliary heating) in a given time step is selected.

In the first part of the paper, the MC-GHP model is described in detail. The compressors are modeled using third order correlations with 10 coefficients obtained from standardized testing under the CAN/ANSI/AHRI 540-2015 standard. Plate heat exchangers models for the evaporator and condenser are also presented. The global model is assembled in the EES software tool which evaluates which compressor should be used at every time step.

Hourly simulations are performed over a three-month period with the Montréal weather, evaluating each compressor individually and using multiple compressors in parallel. Results show that the seasonal coefficient of performance of the MC-GHP is 13.3 % higher than the best heat pump equipped with a single compressor used in this study.

Future work

The EES software provided a good framework for modeling the MC-GHP. However, it would preferable to build a stand-alone TRNSYS model for this type of heat pump in order to facilitate the integration with other established TRNSYS models (building, ground heat exchanger …).

The main source of model uncertainty is related to the calculation of the heat transfer coefficients in the two-phase flow and of the compressor model coefficients. An uncertainty analysis should be performed to ascertain the influence of these individual uncertainties on the overall performance.

Work is also underway to compare the MC-GHP with a single variable speed compressor heat pump. Finally, experimental validation of the proposed model would certainly strengthen this modeling effort.

Acknowledgement

Nomenclature (related to the PHE model)

ϕ = surface enlargement factor

β = chevron angle

Re = Reynolds number ($Re = \rho V D / \mu$)

Nu : Nusselt number ($Nu = h D / k$)

h_{tp} = two phase heat transfer coefficient [W/m^{2}C]

k_{tp} = two phase thermal conductivity [W/m C]

X_m = mean vapor quality

G = mass flux [kg/m^2 s]

G_{eq} = equivalent mass flux [kg/m^2 s]

μ_l = viscosity of the liquid phase [Pa. s]

h = heat transfer coefficient [W/m^{2}C]

q = heat transfer rate [kW]

P_r = actual pressure P over critical pressure P_c

M = molar mass [kg/kmol]

References

AHRI. (2015). Performance Rating of Positive Displacement Refrigerant Compressors and Compressor Units, *Standards Council of Canada*, Standard 540.

Arpagaus, C., F. Bless, S. Bertsch, A. Javed, and J. Schiffmann. (2017). 'Heat Pump driven by a Small-Scale Oil-Free Turbocompressor – System Design and Simulation', 12th IEA Heat Pump Conference.

Bergman, T.L., Lavine, A.S., Incropera, F.P. and D.P. Dewitt. (2011). Fundamentals of Heat and Mass Transfer, *John Wiley,* 7th ed.

Cooper, M. G. (1984). Heat Flow Rates in Saturated Nucleate Pool Boiling-A Wide-Ranging Examination Using Reduced Properties. *Advances in Heat Transfer*, 157-239. Elsevier.

Engineering Equation Solver (EES). (2020). F-chart software, Madison, Wisconsin, v10.644.

Fuentes, E., Waddicor, D. A. and J. Salom. (2016). Improvements in the characterization of the efficiency degradation of water-to-water heat pumps under cyclic conditions, *Applied Energy*, 179: 778-89.

García-Cascales, J. R., Vera-García, F., Corberán-Salvador, J. M. and J. Gonzálvez-Maciá. (2007). Assessment of boiling and condensation heat transfer correlations in the modelling of plate heat exchangers, *International Journal of Refrigeration*, 30: 1029-41.

Hu, B., Xu, S., Wang, R.Z., Lui, H., Han,L., Zhang Z. and H. Li. (2019). Investigation on advanced heat pump systems with improved energy efficiency. *Energy Conversion and Management,* 192:161-170.

Kim, M.B. and C.Y. Park. (2017). An experimental study on single phase convection heat transfer and pressure drop in two brazed plate heat exchangers with different chevron shapes and hydraulic diameters, *Journal of Mechanical Science and Technology*, 31: 2559-71.

Michaud, M., P. Milan Jr. and H.D. Vo. (2016). Low-Cost Rotating Experimentation in Compressor Aerodynamics Using Rapid Prototyping. International Journal of Rotating Machinery, Article ID 8518904, 10 pages.

Rees, S. J. (2016). An introduction to ground-source heat pump technology. in Simon J. Rees (ed.), *Advances in Ground-Source Heat Pump Systems* (Woodhead Publishing).

Saidi, H. (2019). Modélisation de pompes à chaleur à multiples compresseurs, Mémoire de maîtrise, Polytechnique Montréal.

Shen, B., Abdelaziz, O., Baxter, V. and E. Vineyard. (2019). Cold Climate Heat Pump Using Tandem Vapor-Injection Compressors. In *Cold Climate HVAC 2018*, edited by Johansson, Bagge and Wahlström, 429-39. Cham: Springer International Publishing.

Shen, B., Abdelaziz, O., Rice, C. K., and V. D. Baxter. (2016). Cold Climate Heat Pumps Using Tandem Compressors. 2016 ASHRAE Winter Conference, Orlando, FL, USA.

Schiffmann, J. (2014). 'Small-Scale and Oil-Free Turbocompressor for Refrigeration Application', Purdue Conferences, Compressor Engineering.

Wanniarachchi, A., Ratnam, U., Tilton, E . and K. Dutta-Roy. (1995). Approximate correlations for chevron-type plate heat exchangers, *30th National Heat Transfer Conference*, 12: 145-51.

Yan, Y.-Y., Lio, H.-C. and T.-F. Lin. (1999). Condensation heat transfer and pressure drop of refrigerant R-134a in a plate heat exchanger, *International Journal of Heat and Mass Transfer*, 42: 993-1006.

.

Appendix A

The characteristics of the eight compressors used in the present study are shown in Tables A-1 and A-2.

Table A-1 Power input coefficients:

Coeff	1	2	3	4	5	6	7	8
C1	280.8	250.4	-305.6	169.6	157.1	141.8	46.04	334.8
C2	8.164	5.785	1.117	5.662	3.485	3.175	2.421	8.696
C3	0.204	1.284	15.13	-0.05878	0.6986	0.5221	1.74	0.8938
C4	0.09919	-0.02954	0.03343	0.01477	-0.01678	-0.01466	-0.01071	0.05136
C5	-0.02061	0.0721	0.09237	-0.01082	0.04496	0.03754	0.02246	0.01488
C6	0.004531	-0.01824	-0.138	0.001824	-0.01038	-0.008152	-0.01764	-0.007699
C7	0.0003749	0.0001016	0.000372	0.0005202	0.0000602	0.000091	0.00007556	0.0002991
C8	-0.0003008	0.0008938	0.0002431	0.0001293	0.0005378	0.0004525	0.0002989	0.0001441
C9	0.000122	-0.0005201	-0.0004312	0.0000127	-0.0003206	-0.0002679	-0.0001668	-0.0000826
C10	-0.00003852	0.0000709	0.0004111	-0.0000108	0.0000413	0.0000319	0.00005607	0.0000016

Table A-2 Refrigerant mass flow coefficients:

Coeff	1	2	3	4	5	6	7	8
C1	83.86	1017	-254.9	1136	760.2	597.3	491.5	1912
C2	-12.51	3.319	-12.06	26.46	2.261	1.865	6.534	2.315
C3	33.32	15.62	61.23	-8.744	10.84	9.809	2.211	-12.36
C4	1.057	0.2064	0.2259	0.4014	0.1609	0.1318	0.03694	0.879
C5	-0.259	-0.09038	0.496	-0.478	-0.07024	-0.0576	-0.1102	-0.3107
C6	-0.09435	-0.04469	-0.6455	0.1991	-0.02597	-0.02938	0.02747	0.2984
C7	0.0004962	0.0001698	0.001099	0.0008825	0.0001583	0.0001556	0.0006676	-0.004099
C8	-0.008131	-0.001661	-0.0012	-0.003532	-0.001329	-0.001121	-0.0008415	-0.004727
C9	0.003721	0.0008419	-0.002537	0.003186	0.000669	0.0005612	0.0007242	0.002607
C10	0.0005354	0.0006986	0.002803	-0.0005819	0.0004836	0.0004212	0.0001034	-0.0002846